IEEE Access
Multidisciplinary | Rapid Review | Open Access Journal

Received September 11, 2020, accepted October 3, 2020, date of publication October 16, 2020, date of current version October 29, 2020.

Digital Object Identifier 10.1109/ACCESS.2020.3031740

Improving the Quality of Magnetic Signature Reproduction by Increasing Flexibility of Multi-Dipole Model Structure and Enriching Measurement Information

JAROSLAW TARNAWSKI[1], ADAM CICHOCKI[2], TOMASZ ADAM RUTKOWSKI[1], KRYSTIAN BUSZMAN[2], AND MIROSLAW WOLOSZYN[1]

[1]Faculty of Electrical and Control Engineering, Gdańsk University of Technology, 80-233 Gdańsk, Poland
[2]Faculty of Navigation and Naval Weapons, Polish Naval Academy, 81-103 Gdynia, Poland

Corresponding author: Jaroslaw Tarnawski (jaroslaw.tarnawski@pg.edu.pl)

This work was supported in part by the European Defence Agency (EDA) Project, Signature Response Analysis on Multi Influence Sensors II (SIRAMIS II), under Grant B-1469-ESM1-GP.

ABSTRACT The paper presents the construction of a multi-dipole model that allows reproducing magnetic signatures of ferromagnetic objects. The virtual object used in the paper is an ellipsoid, which is the source of synthetic data. To make the situation more realistic, noise is added to the synthetic data. Two significant improvements compared to previous work are presented. Three-axial magnetometers are introduced instead of uniaxial magnetometers. However, a more important change is the modification of the model structure that allows placing dipoles on the entire plane, e.g. object's deck. The multi-dipole model consists of an a priori assumed number of permanent and induced single-dipole models. Each single dipole is described by three magnetic moments and, depending on the applied approach, one or two dipole position parameters. The non-linear least-squares optimization method is used to determine model parameters. To assess the quality of magnetic signature reproduction, qualitative and quantitative forms are used. The final quality assessment is based on differences between the reference fields and the fields determined from the multi-dipole model. The applied modifications bring significant improvement, however, only their combined application allows to restore magnetic signatures with good quality for directions other than for which the data were available.

INDEX TERMS Marine vehicles, magnetic fields, computational electromagnetics, electromagnetic modelling, curve fitting, model checking, synthetic benchmarking, magnetic signatures.

I. INTRODUCTION

All naval objects, such as e.g. ships, which are built or consist of any ferromagnetic elements disrupt natural Earth's magnetic field in their own surrounding. This disorder in the underwater environment is defined as the ship's own magnetic field, identified by its complex magnetic signature [1], [2]. To minimize this magnetic signature, navy ships have a degaussing system, which consists of coils with currents controlled by a specialized controller depending on the ship's course. In this paper, it is assumed that ships do not have any degaussing system. The magnetic signature technology has practical significance for analysing the behaviour of naval ferromagnetic objects in the magnetic field of Earth, e.g. in applications focused on object detection and/or classification, and for the safety of naval transport by reducing ship's risk of being detected by naval mines [3].

The magnetic signature contains two main magnetization components: permanent and induced [1]. The permanent type of magnetization depends on ship size, its ''magnetic history'' (production and storage of ship's sheet metal, and ship's building technology), ferromagnetic properties of sheets, or even mechanical strikes and temperature stresses during exploitation [4]. The induced magnetization is directly related to the current geographical position and orientation (course) of the ship in the Earth's magnetic field - current heading of the ship [4].

Practically, there are two possibilities to acquire the magnetic signature of any type of naval ferromagnetic objects. The most reliable data comes from physical measurements of

The associate editor coordinating the review of this manuscript and approving it for publication was Wen-Sheng Zhao.

a real object. These measurements are typically carried out at the stationary measuring range [3], [5], or by moving sensors mounted on autonomous underwater vehicles [6]. When the real measuring range is not available, numerical simulation should be used as a source of synthetic data for further analyses. Typically, the magnetic signatures are calculated by using a sophisticated FEM method [1], [2], [7]–[11]. Numerical modelling of the magnetic field of the analysed objects, even with software packages, has some limitations related mainly to the small ratio of the thickness of metal sheets used for their construction to their size [8]. That makes it is necessary to use a dense grid with a tremendous number of finite elements. Additionally, the presence of object's permanent magnetism complicates the numerical modelling process and significantly increases the time of numerical calculations. If the course of the object changes, the numerical model must be recalculated.

The 3D ellipsoidal shell geometry used as the case study in this paper is widely accepted as close and appropriate representation of a naval vessel hull [12]–[14]. The simulation results obtained with this model are used in the paper as raw synthetic data from virtual measurements done by multi-axis magnetometers working in the virtual measuring range. The synthetic data was supplemented with noise to bring the simulation scenario closer to the situation in the real measuring range.

In the previously conducted research with the multi-dipole model [15], only the vertical magnetic flux density component B_Z on N and E directions was considered. In that case, the positions of individual dipoles, of permanent and induced nature, were assumed along three main lines: port (P), keel (K), and starboard (S), located at the deck height symmetrically to the ship hull. The magnetic moments and positions of all dipoles were calculated via solving the appropriately defined optimization task with the Levenberg-Marquardt optimization algorithm [15]. The estimation of magnetic dipoles parameters by optimization is also widely used by other authors, e.g. [16]–[19].

In this paper, it is assumed that ship's magnetic data are available on four cardinal courses N, W, S and E. The data related to courses N and E are used for determining multi-dipole model parameters, while the data from the other two courses, S and W, are used to verify the resulting multi-dipole model. Particular point dipoles, of both permanent and induced nature, can be located not only along three main lines P, K and S, but also inside a rectangle on the horizontal plane xy being the approximation enclosing the cross-section of the assumed ellipsoidal shape of the object. A gradient based optimization method with constraints is foreseen for determining magnetic moments and positions of the dipoles in limited ranges. The resulting multi-dipole model needs to be fully verified on a fixed depth in the underwater area and for different courses.

The paper is organized as follows. Section II presents the multi-dipole model, while in Section III, the data gathering procedure based on the object model is described. Section IV gives the description of numerical calculations and their results, including the optimization task formulation and testing scenarios. Finally, Section V concludes the paper. The geometric and magnetic features of the ellipsoidal reference object as the source of synthetic data are given in Appendix.

II. DESCRIPTION OF MULTI-DIPOLE MODEL

In the magnetic dipole theory [20], [21], if the magnetic sensor is located far enough from the ferromagnetic object, at a distance three times larger than the largest dimension of the object, that object may be considered a source of the magnetic field described by the individual magnetic dipole model. However, for typical measuring ranges of naval surface objects, this distance is much smaller than the largest dimension of the object - typically its length.

Hence, it is proposed to use the multi-dipole model, which consist of k dipoles, to describe the magnetic signature of the object as the sum composing the total vector. It is assumed that an appropriate number of m permanent dipoles (DP) and n induced dipoles (DI), where $k = m+n$, represent the complex magnetic signature of the analysed object with satisfactory accuracy.

Two dipole location systems are analysed in the article. The first system, presented in Fig. 1, assumes placing the dipoles only along P, K and S lines, while the other system, shown in Fig. 2 allows an arbitrary position of the dipole within the 2-D area of rectangular approximation of the surface deck (Section VI).

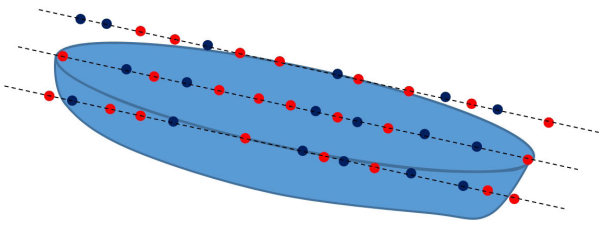

FIGURE 1. Possible dipole locations along keel, port, and starboard sides of the vessel (permanent dipoles - red dots, induced dipoles – blue dots; dotted lines are constraints of dipole locations).

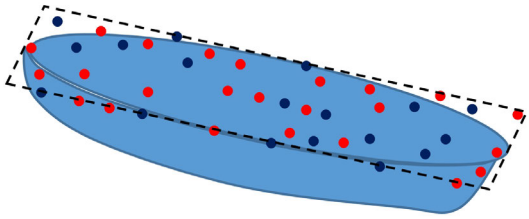

FIGURE 2. Possible dipole locations on the vessel deck surface (permanent dipoles - red dots, induced dipoles – blue dots; rectangular approximation of the deck area as constraint of dipole locations – dotted line).

The multi-dipole model allows flexibility in reconstructing the entire magnetic field disturbance map around the ferromagnetic source object located at the origin of the Cartesian

coordinate system. The vector of magnetic flux density generated at an arbitrary point (x, y, z) by the i-th dipole located at point (x_i, y_i, z_i), can be described as follows [20], [21]:

$$\mathbf{B}_i(\mathbf{M}_i, \mathbf{R}_i) = \frac{\mu_0}{4\pi} \cdot \left(\mathbf{R}_i^T \mathbf{M}_i \mathbf{R}_i \cdot \frac{3}{R_i^5} - \frac{\mathbf{M}_i}{R_i^2} \right), \quad (1)$$

$$\mathbf{B}_i = \begin{bmatrix} B_{x,i} \\ B_{y,i} \\ B_{z,i} \end{bmatrix}, \mathbf{M}_i = \begin{bmatrix} m_{x,i} \\ m_{y,i} \\ m_{z,i} \end{bmatrix}, \mathbf{R}_i = \begin{bmatrix} (x - x_i) \\ (y - y_i) \\ z_i \end{bmatrix}, \quad (2)$$

$$R_i = |\mathbf{R}_i| = \sqrt{(x - x_i)^2 + (y - y_i)^2 + z_i^2}, \quad (3)$$

where

$$i = 1, \ldots, m, m + 1, \ldots, m + n, \quad (4)$$

and $\mu_0 = 4\pi \times 10^{-7}$ H/m is the space permeability, $\mathbf{B}_i$ is the vector of magnetic flux density of i-th magnetic dipole in each orthogonal direction (x, y, z), $\mathbf{M}_i$ is the vector of i-th magnetic dipole moments in each orthogonal direction (x, y, z), and $R_i = |\mathbf{R}_i|$ denotes the distance vector of the analyzed point (x, y, z) from the i-th dipole with coordinates (x_i, y_i, z_i).

When the considered object changes course, the position and magnetic moment of each dipole defined in the model (1)-(4) should be transformed – this is the prediction capability of the proposed model. The concept of transformation of dipole's position is shown in Fig. 3, and appropriate transformation equations are defined as follows:

$$x_i' = x_i \cdot \cos(\varphi) - y_i \cdot \sin(\varphi), \quad (5)$$

$$y_i' = x_i \cdot \sin(\varphi) + y_i \cdot \cos(\varphi), \quad (6)$$

where φ is the course of the object, and x_i' and y_i' denote the transformed coordinates of the i-th dipole (rotation does not change the z coordinate). Fig. 3 shows how the dipole position (x_i, y_i) for direction N (course $\varphi = 0°$) is transformed to the new location (x_i', y_i') in direction $\varphi = 45°$.

As a result of object's course change (5)-(6), the components of each permanent magnetic dipole moment are also changed. The formula describing this transformation in the Cartesian coordinate system for $i = 1,\ldots,m$ can be expressed as follows:

$$\mathbf{M}'_{\mathrm{i}} = \begin{bmatrix} m'_{x,i} \\ m'_{y,i} \\ m'_{z,i} \end{bmatrix} = \begin{bmatrix} m_{xP,i} \cdot \cos(\varphi) - m_{yP,i} \cdot \sin(\varphi) \\ m_{xP,i} \cdot \sin(\varphi) + m_{yP,i} \cdot \cos(\varphi) \\ m_{zP,i} \end{bmatrix}, \quad (7)$$

where indices $m_{xP,i}$, $m_{yP,i}$ and $m_{zP,i}$ denote the components of permanent magnetic dipole moments in orthogonal x,y,z directions.

Notice that theoretically, the values of permanent magnetic moments of the identified dipoles do not change at the new geographical position of the object and depend only on its course φ. In practice, real changes of those values for individual objects are unknown and require new measurements for their identification.

The values of induced magnetic moments of the considered induced dipoles are directly related to the geographical position and course of the object. Taking into account the object approximation having the geometrical form of 3D longitudinal ellipsoidal shell (Fig. 4), the transformation formulas for components of each i-th induced magnetic dipole moment $(i = m + 1, \ldots, m + n)$ are given as follows [12]:

$$m'_{x,i} = B_{xE,i} \cdot (f_1 + f_{31} \cdot \sin^2(\theta) \cdot \cos^2(\varphi)) + \ldots$$
$$\ldots + B_{zE,i} \cdot (f_{31} \cdot \cos(\theta) \cdot \sin(\theta) \cdot \cos(\varphi)), \quad (8)$$

$$m'_{y,i} = B_{xE,i} \cdot (f_{31} \cdot \sin^2(\theta) \cdot \sin(\varphi) \cdot \cos(\varphi)) + \ldots$$
$$\ldots + B_{zE,i} \cdot (f_{31} \cdot \cos(\theta) \cdot \sin(\theta) \cdot \sin(\varphi)), \quad (9)$$

$$m'_{z,i} = B_{xE,i} \cdot (f_{31} \cdot \cos(\theta) \cdot \sin(\theta) \cdot \cos(\varphi)) + \ldots$$
$$\ldots + B_{zE,i} \cdot (f_1 + f_{31} \cdot \cos^2(\theta)), \quad (10)$$

where $B_{xE,i}$, $B_{yE,i}$, and $B_{zE,i}$ are the components of the vector of ambient Earth magnetic flux density $\mathbf{B}_{\mathrm{E}}$ at the location of i-th induced dipole, and the values of factors f_1 and f_{31} depend on shape and size of the ellipsoidal object (Appendix).

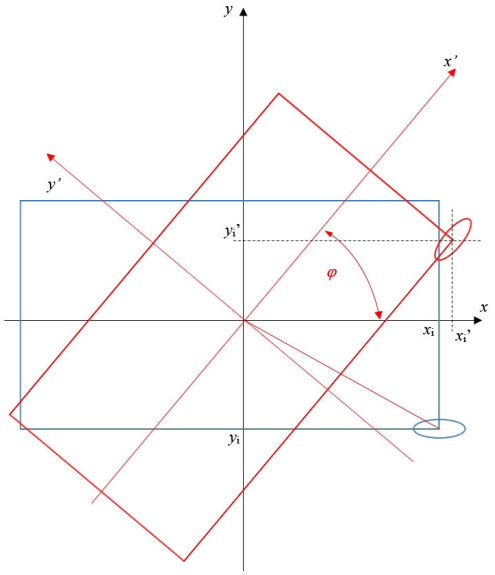

FIGURE 3. Concept of dipole position transformation.

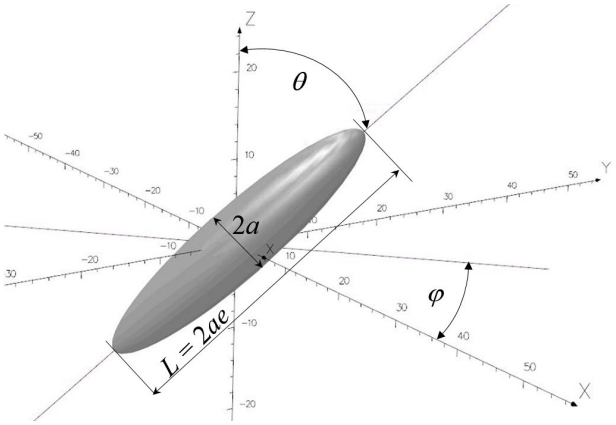

FIGURE 4. Virtual ferromagnetic object – longitudinal ellipsoidal shell.

TABLE 1. Ellipsoid geometric and magnetic parameters.

Symbol	Quantity	Value
L	ellipsoid length	48 m
$D=2a$	ellipsoid diameter	8 m
e	ratio of length L to diameter D	6
φ	object course	0°, 90°, 180°, 270°
θ	inclination angle to xy plane	90°
B_E	External Earth magnetic field	50 μT
B_{xE}	x component of external magnetic field	17101 nT
B_{yE}	y component of external magnetic field	0 nT
B_{zE}	z component of external magnetic field	46985 nT
m_{xP}	permanent x component of ellipsoid's magnetic moment	80424 Am^2
m_{yP}	permanent y component of ellipsoid's magnetic moment	-4400 Am^2
m_{zP}	permanent z component of ellipsoid's magnetic moment	-31415 Am^2
m_{xI}, $\varphi=0°$	induced x component of ellipsoid's magnetic moment for φ = 0°	31415 Am^2
m_{zI}, $\varphi=0°$	induced z component of ellipsoid's magnetic moment for φ = 0°	-123115 Am2
m_{yI}, $\varphi=90°$	induced y component of ellipsoid's magnetic moment for φ = 90°	44810 Am^2
μ_r	relative magnetic permeability of object's material	100

While, all parameters, geometric and magnetic, of the 3D longitudinal ellipsoidal shell geometry are given in Table 1.

Taking into account that for naval surface objects, the angle θ is equal to 90° and the horizontal position of the object is the water surface, Equations (8)-(10) can be written in the following compact form:

$$\mathbf{M}'_{\mathrm{i}} = \begin{bmatrix} m'_{x,i} \\ m'_{y,i} \\ m'_{z,i} \end{bmatrix} = \begin{bmatrix} B_{xE,i} \cdot (f_1 + f_{31} \cdot \cos^2(\varphi)) \\ B_{xE,i} \cdot f_{31} \cdot \sin(\varphi) \cdot \cos(\varphi) \\ B_{zE,i} \cdot f_1 \end{bmatrix}. \quad (11)$$

and after further transformations, they can be presented as

$$\mathbf{M}'_{\mathrm{i}} = \begin{bmatrix} m'_{x,i} \\ m'_{y,i} \\ m'_{z,i} \end{bmatrix} = \begin{bmatrix} m_{I1,i} + m_{I2,i} \cdot \cos^2(\varphi) \\ m_{I2,i} \cdot \sin(\varphi) \cdot \cos(\varphi) \\ m_{I3,i} \end{bmatrix}, \quad (12)$$

where $m_{I1,i}$, $m_{I2,i}$, and $m_{I3,i}$ are the aggregated components of the induced magnetic dipole moments, such that:

$$m_{I1,i} = B_{xE,i} \cdot f_1, m_{I2,i} = B_{xE,i} \cdot f_{31}, m_{I3,i} = B_{zE,i}. \quad (13)$$

Notice that considering possible k=m+n locations of dipoles on the object deck surface, the independent variables in the presented multi-dipole model, Eq. (1-7) and (13), are magnetic moments $m_{x,i}$, $m_{y,i}$, $m_{z,i}$ of the dipoles and their locations x_i and y_i on the horizontal plane xy (i = 1,…,k) – i×5 independent variables in total. The magnetic moments of the dipoles can have permanent $m_{xP,i}$, $m_{yP,I}$, $m_{zP,i}$ (7) or induced nature $m_{I1,i}$, $m_{I2,i}$, $m_{I3,i}$ (12).

The locations and values of the permanent and induced magnetic moments of the dipoles are determined once based on the magnetic flux density data (Section III), by solving the inverse optimization problem (Section IV) with the multi-dipole model described in that section.

III. ORIGIN OF MAGNETIC SIGNATURES

Technically, there are two possibilities to acquire the magnetic signature of any naval ferromagnetic object of arbitrary type: by measurements on a real object, or by numerical modelling and simulations of the magnetic field surrounding the analysed object. The real measurements may be done with magnetometers mounted in line, cross, or array configuration at some depth under water surface, in the stationary measuring range - Fig. 5. The magnetometers can be of scalar (total) type, or multi-axis vector magnetometers. In the former case, the module of the magnetic flux density is measured, while in the latter, all three components of magnetic flux density are available. Typically, multi-axis sensors are used, e.g. magnetometer Mag-03 [22]. Specific configuration of magnetometer locations allows to measure part of magnetic signature of the object in two or four basic magnetic directions. To get the magnetic data, it is necessary for the object to pass the measuring range in the specific place and with specific course (direction).

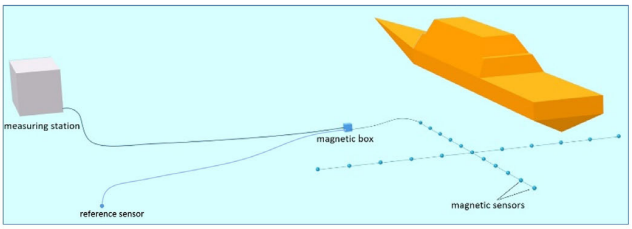

FIGURE 5. Example of the measuring range with cross configuration of magnetic sensors.

The structure of the data delivered by each multi-axis sensor can be described as follows:

$$\mathbf{B}_M = \mathbf{B}_E + \mathbf{e}_E + \mathbf{B}_A + \mathbf{e}_M = \mathbf{B}_E + \mathbf{B}_A + \mathbf{e}_{EM}, \quad (14)$$

where $\mathbf{B}_M$ is the vector of magnetic flux density components $[B_{xM}, B_{yM}, B_{zM}]^{\mathrm{T}}$ measured in each orthogonal direction, $\mathbf{B}_E$ is the vector of natural Earth magnetic flux density components $[B_{xE}, B_{yE}, B_{zE}]^{\mathrm{T}}$, $\mathbf{e}_E$ is the vector of noise components $[e_{xE}, e_{yE}, e_{zE}]^{\mathrm{T}}$ in the ambient Earth magnetic flux density, $\mathbf{B}_A$ is the vector of magnetic flux density anomaly components $[B_{xA}, B_{yA}, B_{zA}]^{\mathrm{T}}$ – being the distortion in natural Earth magnetism caused by the presence of the ferromagnetic object, $\mathbf{e}_M$ is the vector of measuring noise components $[e_{xM}, e_{yM}, e_{zM}]^{\mathrm{T}}$, and $\mathbf{e}_{EM}$ is the vector of aggregated $\mathbf{e}_E$ and $\mathbf{e}_M$ noise components. Notice that the noise $\mathbf{e}_E$ can be much higher than the measuring noise $\mathbf{e}_M$, but it can be significantly minimized when sensor measurements are compensated by an additional reference magnetometer located far enough from the measuring range [8]. The number of sensors, along with their arrangement and covered area, are an essential aspect of each measuring field structure.

For the simulation studies described in the paper, the access to the data from a virtual, simulated measuring range with three three-axis magnetometers in each direction (working in the cross configuration) was assumed. Such magnetic data with additional noise, according to Scheme (14), was used as synthetic data for further analysis with a multi-dipole model.

The 3D longitudinal ellipsoidal shell was selected as the case study naval object and modelled (Section II, Appendix). Hence, it is possible to get a complex magnetic signature of that object in the form of a complete map of the magnetic field at each point around it, and in the form of partial magnetic signature related to the sensor location. In that latter case, the simulation of object passing the measuring range in specific direction can be performed and the virtual measurement data can be acquired. On the other hand, the necessary synthetic magnetic data can be generated taking into account that the object is static and located at the centre of the measuring range system. This solution was selected in the paper.

The calculations of the magnetic field are based on the analytical model of the 3D longitudinal ellipsoidal shell, which detailed description of may be found in e.g. [13]. Additionally, it is assumed that the size of the measurement area is from -100 m to 100 m, and the measurement resolution is 1 m. The data are acquired on three lines related to object geometry, which are: port (P), keel (K) and starboard (S) lines, (Fig. 6).

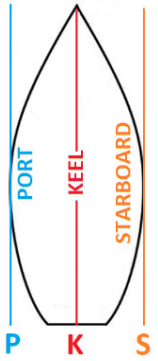

FIGURE 6. Sides and keel of the object determining the location of P, K and S lines.

In general, it is assumed that the object may pass the measurement range in four cardinal directions, course N (North, $\varphi = 0°$), course W (West, $\varphi = 90°$), course S (South, $\varphi = 180°$), and course E (East, $\varphi = 270°$), see Fig. 7.

Notice that in the presented paper, the authors do not consider the optimal measuring range configuration, the number of measuring paths and the distance between them. In the comparison to the previously conducted research [15] in the presented paper analyses whether replacement of scalar to three-axis magnetometers and the multi-dipole model structure modification will enable the reconstruction of magnetic signatures with greater accuracy than before.

In the simulation studies, the data from courses N and E were used as the source data to identify, via optimization, the

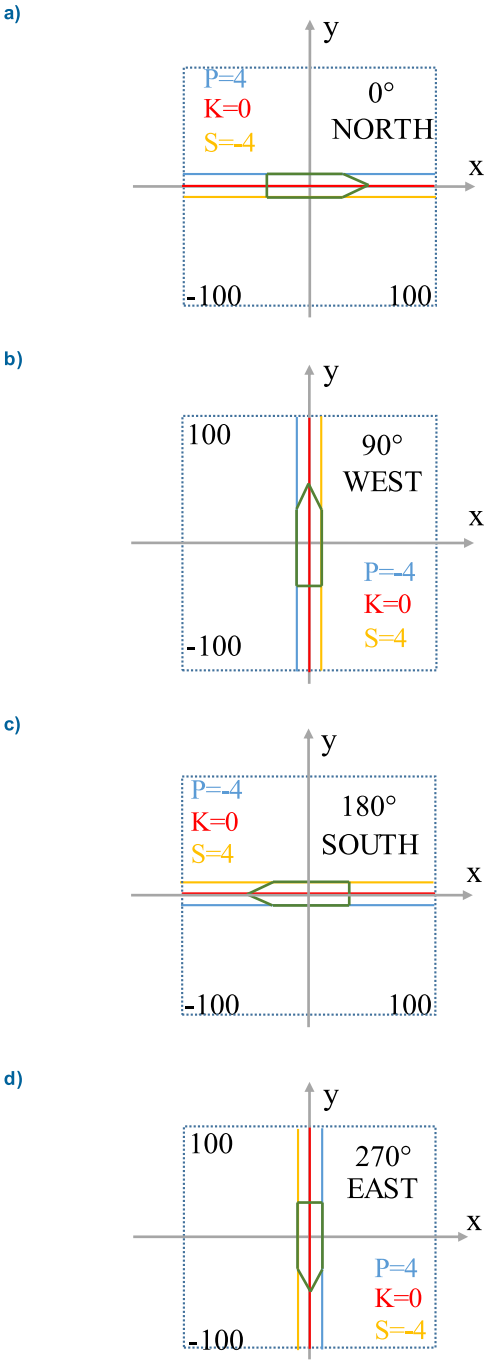

FIGURE 7. Location of sides and keel of the ship for different courses: a) NS (North); b) WE (West); c) SN (South); d) EW (East).

multi-dipole model, while the data from the remaining two courses, S and W, were used to verify the quality of the resulting multi-dipole model. These two aspects: identification and verification of multi-dipole model parameters, are described in detail in Section IV.

The sample data used in the identification of multi-dipole model parameters is presented in Fig. 8. At the depth of -20 m, the component *By* of magnetic flux density in direction 0 is intersected at P, K and S coordinates according

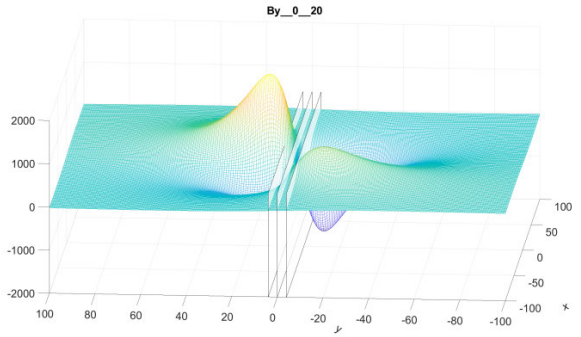

FIGURE 8. Field of By component expressed in nT, with cutting planes along P, K and S coordinates.

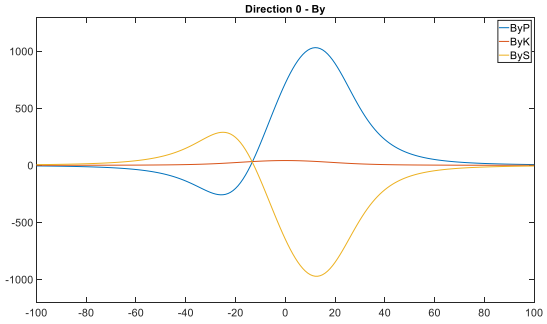

FIGURE 9. PKS paths cut from By component of magnetic flux density.

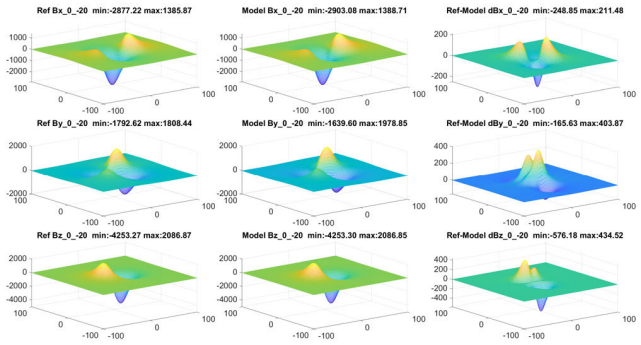

FIGURE 10. Ref-model differences on fields in nT: direction 0.

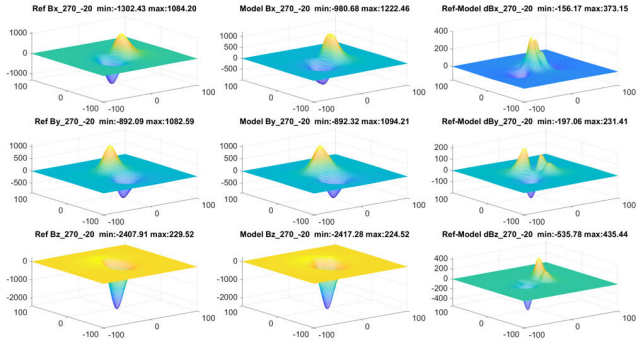

FIGURE 11. Ref-model differences on fields in nT: direction 270.

to Fig. 6. As a result of this operation, the paths shown in Fig. 9 are created. From the modelling point of view, using paths instead of fields is a significant limitation of input information to the model. However, it was done intentionally to comply with the modelling approach based on the possessed measurement data.

IV. NUMERICAL CALCULATIONS

The calculations consisted of two stages. The first stage was the optimization procedure to determine parameters of the multi-dipole model based on P, K and S path data, while the second stage involved reproduction of the magnetic signature based on the multi-dipole model. The magnetic signature was obtained in the form of fields of magnetic components B_x, B_y, B_z expressed in nT.

A. PREVIOUS RESULTS

The first undertaken computational task was to reproduce the results from the experiment described in [9]. This was not entirely possible due to the fact that a real object was used in that case. Nevertheless, the approach to the model building process was fully mapped. The results (Fig. 10 - 11) obtained when reproducing the previously conducted experiment with present synthetic data was then used as a reference for comparison with the currently proposed solutions.

Comparing qualitatively the charts of the left and middle columns in Figs. 10 - 11, it can be stated that the degree of mapping is high. Also, the results on the paths for the

TABLE 2. Numerical simulation scenarios.

Scenario	Data	Y-coord	Noise
Scenario S0 (base)	Bz	PKS	0
Scenario S1	Bx, By, Bz	PKS	0
Scenario S2	Bz	free	0
Scenario S3	Bx, By, Bz	free	0
Scenario S4	Bx, By, Bz	free	+/- 1 nT

Bz component presented in Figs. 12 - 18 show a good fit. However, quantitative differences between the reference and model fields, shown in the right column in Figs. 10 - 11 indicates significant modelling errors. Hence the conviction that there was a need to streamline the process of building the model in order to improve its quality of magnetic signature reproduction.

B. NUMERICAL SIMULATION SCENARIOS

To clearly analyse and present the impact of each modernization on the final result, a number of simulation scenarios have been developed, as summarized in Table 2. Scenario S0 consists in mapping the experiments from the previous article with current data. Scenarios S1 and S2 contain modernization proposals consisting in, respectively, enriching the measurement information, and increasing the structure's flexibility. Scenario S3 is a combination of the above upgrades, while

Scenario S4 takes additionally into account the noise that may arise during real measurements.

C. OPTIMIZATION PROBLEM FORMULATION

The task of the optimization procedure is to minimize the distance between the reference and model data on P, K and S tracks. Hence, the appropriate optimization problem for a priori chosen number of m permanent dipoles and n induced dipoles is defined as follows:

$$\min_{\Omega\in\{\Omega_1,\ldots,\,\Omega_{n+m}\}} J_G = \sum_{l}\sum_{k}\sum_{d}\sum_{j=-100}^{100} \times \left(B_{l,d}^{ref}(j,k) - B_{l,d}^{model}(j,k,\Omega)\right)^2 \tag{15}$$

$$\text{subjectto}: \underset{i\in(1,m+n)}{\forall} \Omega_i^{\min} \le \Omega_i \le \Omega_i^{\max} \tag{16}$$

where

$$\underset{i\in(1,m+n)}{\forall} \Omega_i \in \left\{m_{x,i}, m_{y,i}, m_{z,i}, x_i, y_i\right\}, \tag{17}$$

$$l \in \{x, y, z\}, \tag{18}$$

$$k \in \{P, K, S\}, \tag{19}$$

$$d \in \left\{0^\circ,\ 270^\circ\right\}, \tag{20}$$

and $\Omega_i^{\min}$, $\Omega_i^{\max}$ are the vectors of minimal and maximal constraint values for the decision variables related to the *i-th* considered dipole.

The objective function J_G (15) defines the difference in matching the reference and model data in all considered directions, for paths P, K and S (19), over the length of 200 m, with the resolution of one meter for magnetic field components B_x, B_y, B_z (17). Depending on the simulation scenario, the objective function takes a different form. Inside the criterion function, there is the sum of squares of model and source data differences for individual magnetic field components. In Scenarios 0 and 2, this will be only the B_z component, while in the remaining scenarios it will be B_x, B_y, B_z. The number of decision variables depends on whether the location of dipoles is only imposed on P, K and S lines, or it is possible to place dipoles at arbitrary points on the plane. In the former case, 4 parameters (m_x, m_y, m_z, x) are necessary to describe one dipole, while in the latter case 5 parameters (m_x, m_y, m_z, x, y) - (17).

To solve the above optimization task (15-20), a nonlinear least-squares (nonlinear data-fitting) algorithm implemented in the *lsqnonlin* function from the Matlab Optimization toolbox was selected [23]. This function has the ability to take into account constraints (16), which allows to control the position of dipoles and impose range restrictions on magnetic moments. Mentioned constraints were used in a uniform manner to all $m + n$ dipoles, m permanent and n induced dipoles – Table 3.

The structure of the model is determined, among others, by the number of dipoles. For Scenarios 0 and 2, where dipoles are located on P, K and S lines, the number of dipoles was determined according to the principle of 4 permanent and 4 induced dipoles for each line, i.e. the model was described by 24 dipoles in total. In the scenarios with free dipole position in y direction on the plane, the model structure included 10 permanent and 10 induced dipoles.

TABLE 3. Constraints for each i-th dipole in multi-dipole model.

	[m_x,	m_y,	m_z,	x,	y]
$\Omega^{\min}$	[-10e6,	-10e6,	-10e6,	-4,	-24]
$\Omega^{\max}$	[10e6,	10e6,	10e6,	4,	24]

The main idea was that the number of dipoles was similar to the previously conducted research with the multi-dipole model [15]. This article does not consider the minimal, optimal number of dipoles sufficient to describe and reconstruct the magnetic signature. Still, it is certainly an interesting aspect of the application of the multi-dipole model.

Generally, determining the values of the proposed multi-dipole model parameters using optimization can be carried out in at least two ways. The first one, generally called regularization, consists in introducing certain constraints and relationships between the dipoles into the optimization problem (15-20). This approach to the location of dipoles can be found in the previous paper [15], where the data were located along the PKS lines. However, it is not easy to determine the relationship between the values of the magnetic moments. In this article, a different solution was adopted, i.e. the freeing of the dipole positions and the lack of dependence of the magnetic moments. Therefore, the optimization with conservative box constraints (Table 3) for all dipoles locations and its magnetic moments was proposed to solve the problem defined in the paper. Limiting the field of occurrence of dipoles to the deck area seems natural, and the limitation of the magnetic moments has been treated liberally, i.e. in the range of +/- 10e6 Am^2, based on the observation of many typical naval ferromagnetic objects modelled with the use of the multi-dipoles model.

D. SIMULATION RESULTS

The result of the optimization procedure is obtained as the list of model parameter values. Depending on the scenario, it will be $24{\cdot}4 = 96$ or $20{\cdot}5 = 100$ parameters. These values are not explicitly presented in the article because it is difficult to deduce from them. However, these values were used in the multi-dipole model to reproduce the magnetic field components. These results are comprehensively presented in Figs. 12 - 51 and, for the convenience of the reader, collated in Table 4.

The results of individual simulation scenarios can be compared qualitatively in the form of graph observations, and quantitatively in the form of RMSE (root mean square error) and MAE (mean absolute error) fit indicators on paths, as well as by comparing the maximum modelling errors. The root

TABLE 4. Numerical simulation results.

De-pth	Direction [degrees]	RMSE, MAE [nT]	Bx min, max dBx min,max [nT]	By min, max dBy min,max [nT]	Bz min, max dBz min,max [nT]
SCENARIO 0: 2 directions, Bz only, y along PKS, base scenario					
-20	0	54.26,	-2903, 1388	-1639,1978	-4253, 2087
		21.34	-248.8, 211.4	-165.6, 403.9	-576,2,434.5
-20	90	150.26,	-1966, 1088	-1361, 1035	-2889, 552
		73.76	-747.3,369.44	-632.4,356.3	-838.1,787,8
-20	180	147.44,	-2076, 1075	-1715, 1258	-3317,1190
		72.85	-324.6,614.7	-720.6, 374.8	-800.6,734.8
-20	270	49.97,	-980,1222	-892, 1094	-2417, 224
		19,67	-156.2,373.1	-197.1,231.4	-535.8,435.44
SCENARIO 1: 2 directions, Bx,By,Bz, y along PKS; measurement enrichment					
-20	0	0.13,	-2877, 1385	-1793, 1810	-4253,2086
		0.08	-2.38, 4.84	-2.03, 3.3	-4.47, 5.86
-20	90	108.48,	-1614, 1200	-1255, 980	-2798, 279
		56.45	-409.7,417	-350, 326	-442.6, 421.3
-20	180	108.48,	-2086, 1087	-1476, 1459	-3289, 1193
		56.46	-324.2, 350.7	-409.7, 417	-441.9, 420.4
-20	270	0.1187,	-1300, 1084	-892, 1083	-2408, 232
		0.0719	-2.1, 2	-3.1, 3.9	-4.7, 3.7
SCENARIO 2: 2 directions, Bz only, y free; upgraded model structure flexibility					
-20	0	0.7473,	-2877, 1385	-1795, 1808	-4253, 2086
		0.3086	-8.23, 7.2	-6.56, 3.26	-7.8, 10.39
-20	90	18.41,	-1334, 1061	-1090, 895	-2409, 272
		9.0783	-78.36, 75.81	-76.4, 75.81	-83.05, 83.23
-20	180	18.414,	-2059, 1132	-1495, 1489	-3370, 1204
		9.0799	-75.94, 76.41	-78.71, 75.4	-82.83, 83,49
-20	270	0.66795,	-1299, 1083	-892, 1082	-2408, 233
		0.27204	-6.07, 3.33	-7.65, 8.49	-8.93, 9.91
SCENARIO 3: 2 directions, Bx, By, Bz, y free, both improvements					
-20	0	0.0107,	-2877, 1385	-1792, 1808	-4253, 2086
		0.0077	-0.15, 0.4	-0.17,0.33	-0.24, 0.52
-20	90	4.7452,	-1334, 1071	-1086, 893	-2421, 246
		2.2925	-20.28, 19.30	-19.58, 19.51	-21.81, 21.64
-20	180	4.7453	-2060, 1134	-1499, 1486	-3376, 1210
		2.2929	-19.49, 19.61	-20.27, 19.3	-21.87, 21.58
-20	270	0.010404	-1302, 1084	-892, 1082	-2407, 229
		0.007872	-0.14, 0.33	-0.4, 0.16	-0.27, 0.5
SCENARIO 4: 2 directions, Bx, By, Bz, y free, noise 1					
-20	0	0.17649,	-2877, 1385	-1792, 1807	-4252, 2087
		0.11558	-1.8, 2.2	-3.5, 1.6	-4.5, 3.6
-20	90	40.373,	-1406, 1086	-1130, 924	-2490, 207
		20.9545	-148.9, 160.2	-114.2, 116.4	-158.9, 156.5
-20	180	40.3226,	-2063, 1134,	-1501, 1487	-3377, 1225
		20.9346	-117.4, 112.8	-148.4, 159.8	-159.3, 155.3
-20	270	0.16474,	-1304, 1082	-892, 1082	-2407, 228
		0.11168	-3.4, 1.5	-2.6, 1.4	-4.2, 3.7

mean square error is given as

$$RMSE = \sqrt{\frac{1}{N}\sum_{i=1}^{N}(ref_i - model_i)^2}, \tag{21}$$

and the mean absolute error is given as

$$MAE = \frac{1}{N}\sum_{i=1}^{N}|ref_i - model_i|, \tag{22}$$

where $model_i$ is the vector of N signature values at i-th position coordinate counted by the model, and ref_i is the vector of N reference signature values at the same position.

In Scenarios S0-S4, the calculations were conducted on directions N and E, while the results presented on directions W and S can be treated as an assessment of the possibility to reproduce magnetic signatures in directions for which no calculations were carried out.

V. CONCLUSION

Comparing the simulation scenario 1 against 0, a significant improvement can be noticed in matching on both paths and fields for directions 0 and 270, i.e. those for which the calculations were carried out. Therefore, the enrichment of measurement information consisting in the use of a three-axis magnetometer brought the expected improvement.

Comparing the simulation scenario 2 against 0, it can be seen that the release of dipole position has a huge positive impact on the quality of the fit on paths and fields. This improvement can be seen not only on directions 0 and 270, but also on 90 and 180. When deciding initially to make the structure more flexible, the authors expected some improvement, but its scale is impressive.

Comparing the simulation scenario 3 against 0, i.e. using both presented improvements: making the structure more flexible and enriching the measurement information, we get excellent matching results on paths and fields in directions 0 and 270, and definitely the best of all scenarios in other directions.

Adding the noise to the source data, which was supposed to represent the measurement error, did not cause significant deterioration of the results when the noise had values from the range of real measuring devices. On the other hand, the measurement noise simulated at a level significantly greater than the real measurement error of magnetometers has visibly caused a significant degradation of results.

Summing up, the proposed modernization of the approach to the construction of the multi-dipole model in the form of using three-axis magnetometers and making the model structure more flexible have brought great improvement in magnetic signature reproduction. Further work will be undertaken to obtain magnetic signature reproduction in any direction and depth, and to reduce model's sensitivity to noise.

APPENDIX

The factors f_1 and f_{31} introduced in Eq. (8-13) in Section II are defined as follows [12]:

$$f_1 = \frac{\mu_r - 1}{1 + A_1 \cdot \frac{\mu_r - 1}{2}}, \quad f_3 = \frac{\mu_r - 1}{1 + A_3 \cdot \frac{\mu_r - 1}{2}}, \tag{23}$$

$$f_{31} = f_3 - f_1, \tag{24}$$

where

$$A_1 = \frac{e \cdot (e + E)}{e^2 - 1}, \quad A_3 = \frac{-2 \cdot (1 + e \cdot E)}{e^2 - 1} \tag{25}$$

$$E = \frac{\ln\left(e - \sqrt{e^2 + 1}\right)}{\sqrt{e^2 - 1}}, \tag{26}$$

and e is the ratio of length L to diameter D of the ellipsoid, and A_1, A_2, E are demagnetizing coefficients for shape effects.

A. SCENARIO 0: N, E–DIRECTION, B_Z DATA ONLY, Y-COORD ALONG PKS

See Figure 12 to 19 here.

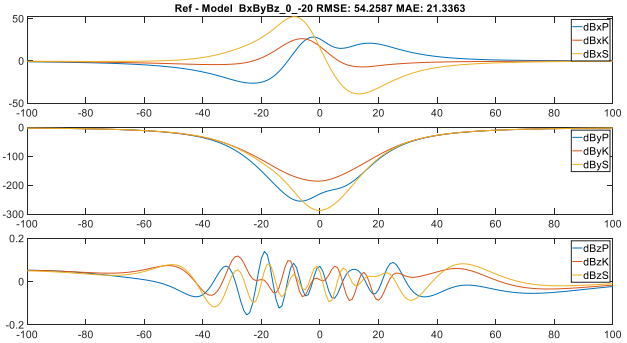

FIGURE 12. Ref-model differences on paths in nT: S0, direction 0.

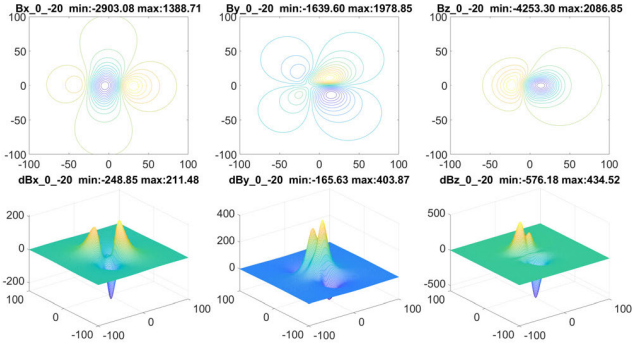

FIGURE 13. Ref-model differences on fields in nT: S0, direction 0.

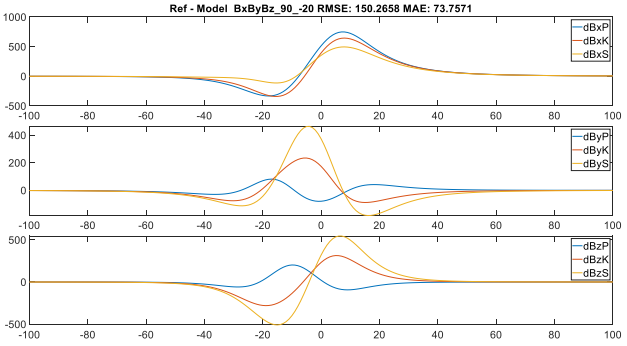

FIGURE 14. Ref-model differences on paths in nT: S0, direction 90.

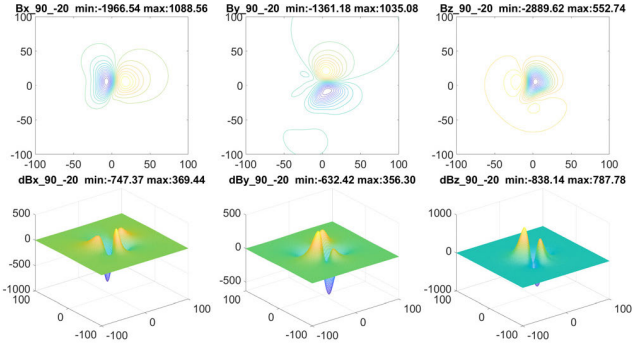

FIGURE 15. Ref-model differences on fields in nT: S0, direction 90.

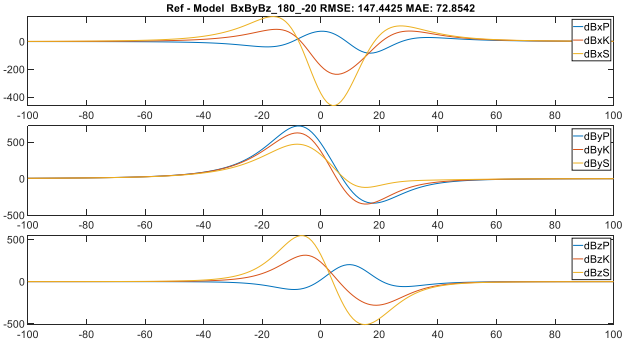

FIGURE 16. Ref-model differences on paths in nT: S0, direction 180.

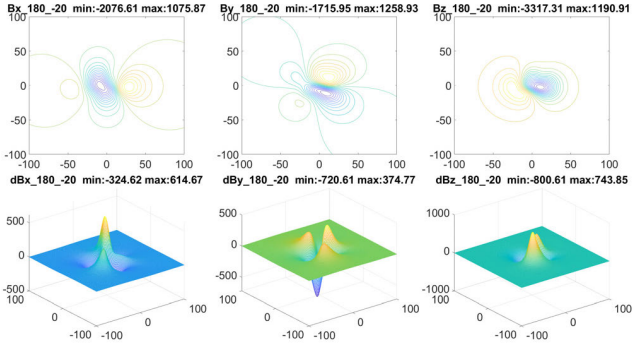

FIGURE 17. Ref-model differences on fields in nT: S0, direction 180.

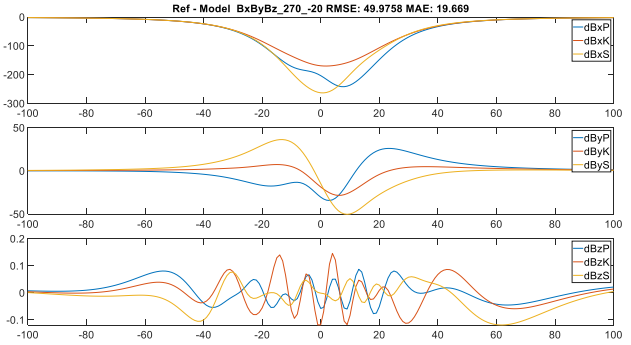

FIGURE 18. Ref-model differences on paths in nT: S0, direction 270.

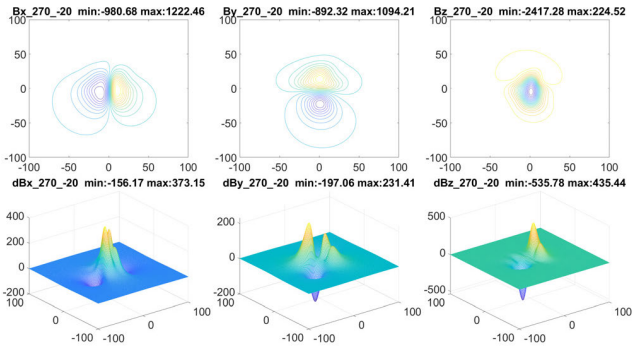

FIGURE 19. Ref-model differences on fields in nT: S0, direction 270.

B. SCENARIO 1: N, E–DIRECTIONS, B_X, B_Y, B_Z DATA, Y-COORD ALONG PKS

See Figure 20 to 27 here.

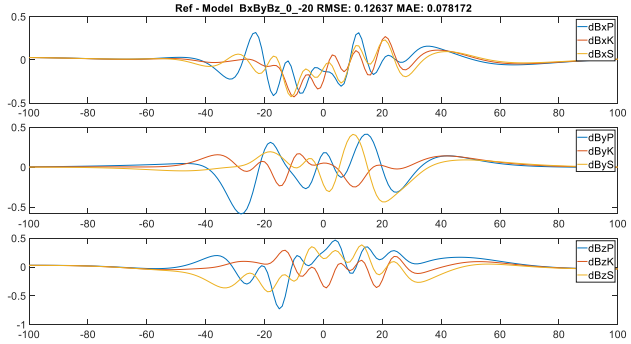

FIGURE 20. Ref-model differences on paths in nT: S1, direction 0.

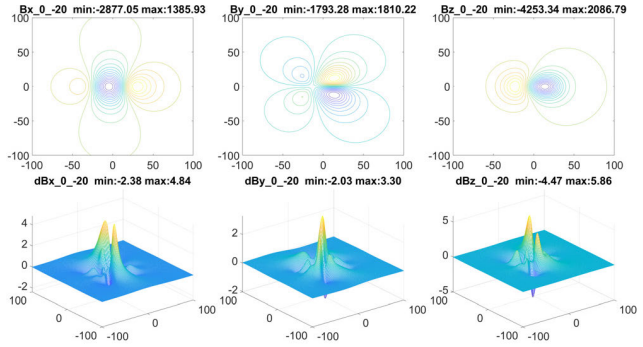

FIGURE 21. Ref-model differences on fields in nT: S1, direction 0.

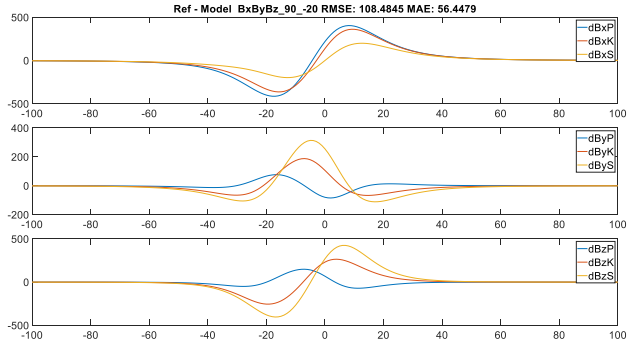

FIGURE 22. Ref-model differences on paths in nT: S1, direction 90.

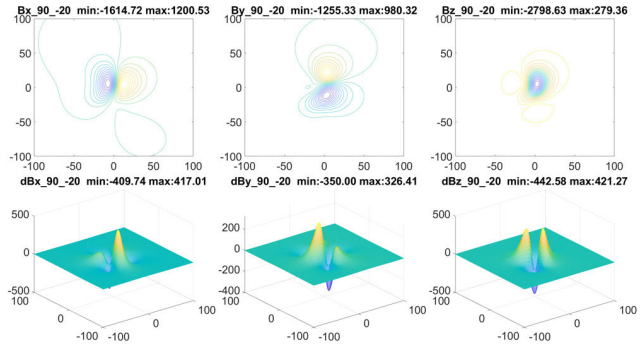

FIGURE 23. Ref-model differences on fields in nT: S1, direction 90.

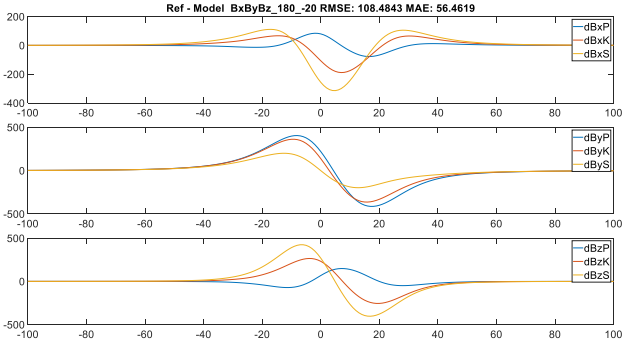

FIGURE 24. Ref-model differences on paths in nT: S1, direction 180.

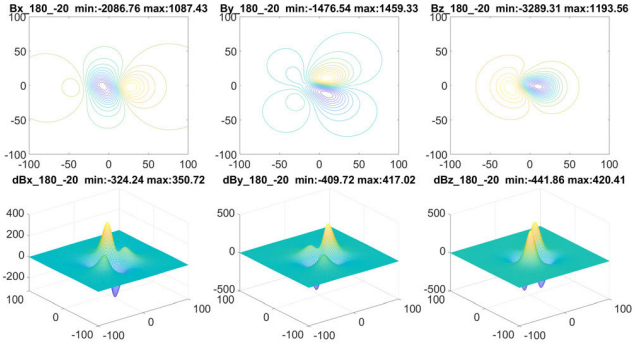

FIGURE 25. Ref-model differences on fields in nT: S1, direction 180.

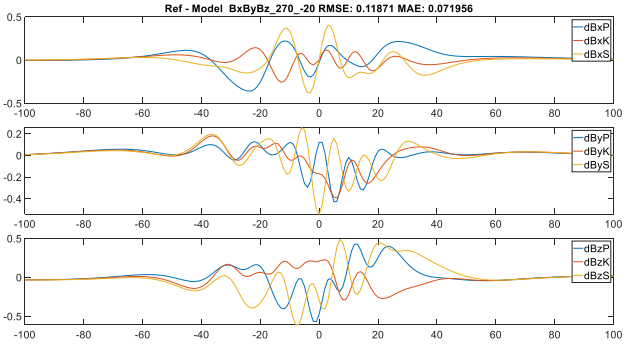

FIGURE 26. Ref-model differences on paths in nT: S1, direction 270.

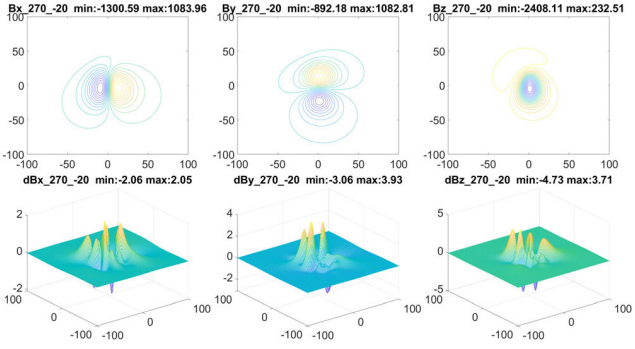

FIGURE 27. Ref-model differences on fields in nT: S1, direction 270.

C. SCENARIO 2: N, E–DIRECTIONS, B_Z DATA ONLY, Y-COORD FREE

See Figure 28 to 35 here.

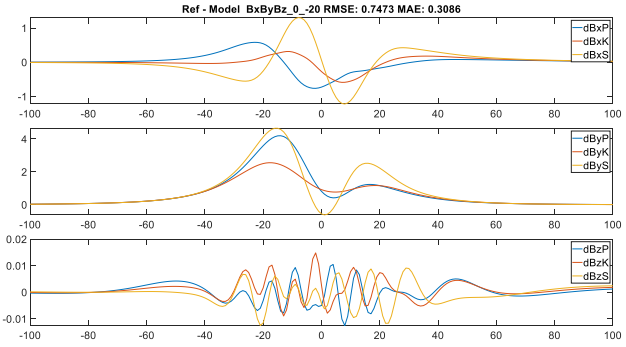

FIGURE 28. Ref-model differences on paths in nT: S2, direction 0.

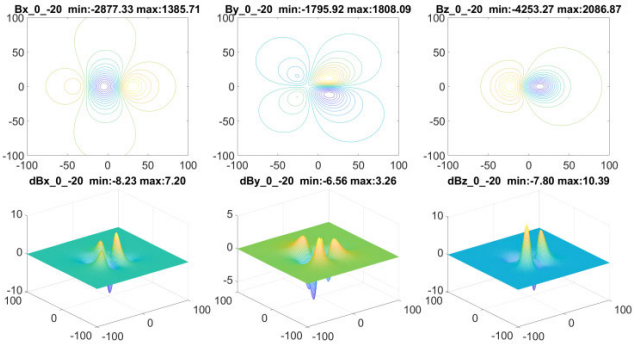

FIGURE 29. Ref-model differences on fields in nT: S2, direction 0.

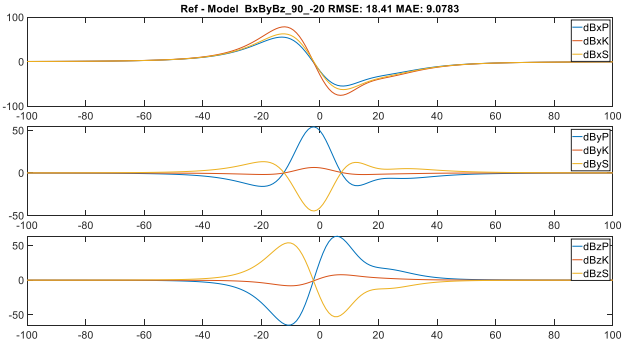

FIGURE 30. Ref-model differences on paths in nT: S2, direction 90.

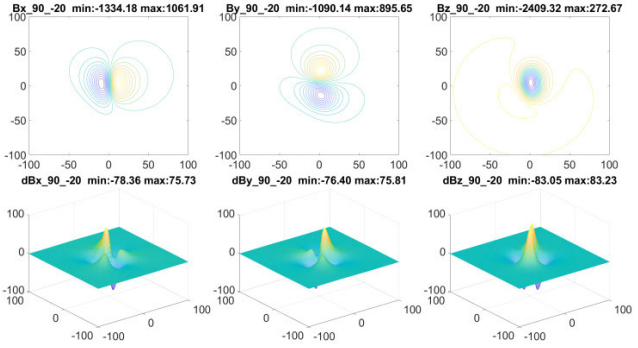

FIGURE 31. Ref-model differences on fields in nT: S2, direction 90.

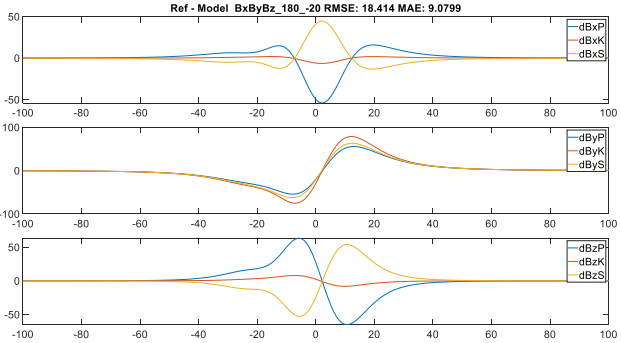

FIGURE 32. Ref-model differences on paths in nT: S2, direction 180.

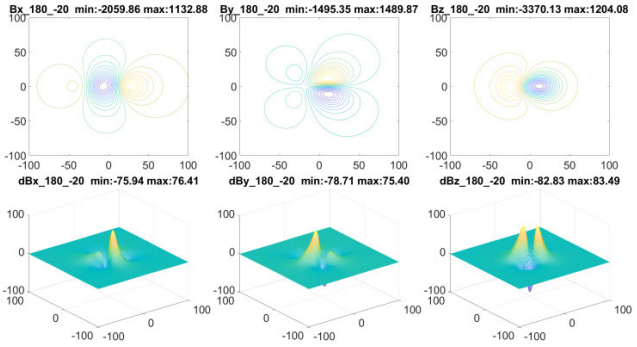

FIGURE 33. Ref-model differences on fields in nT: S2, direction 180.

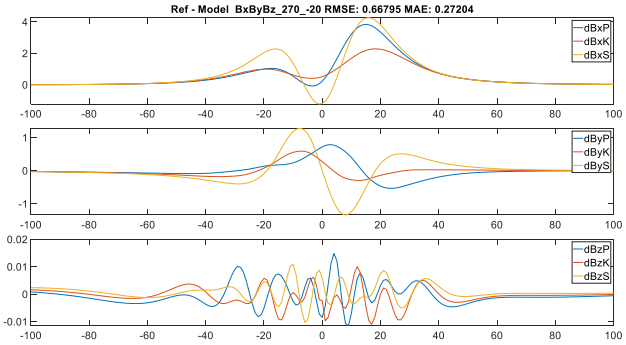

FIGURE 34. Ref-model differences on paths in nT: S2, direction 270.

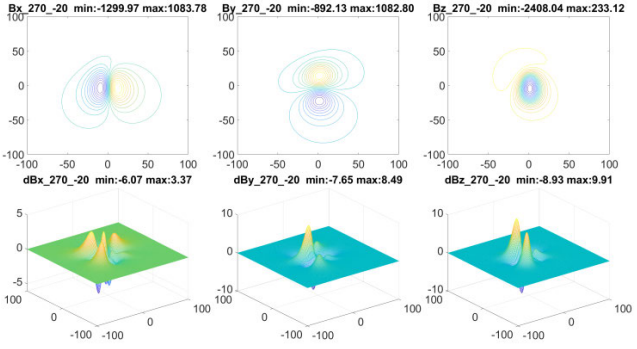

FIGURE 35. Ref-model differences on fields in nT: S2, direction 270.

D. SCENARIO 3: N, E–DIRECTIONS, B_X, B_Y, B_Z DATA, Y-COORD FREE

See Figure 36 to 43 here.

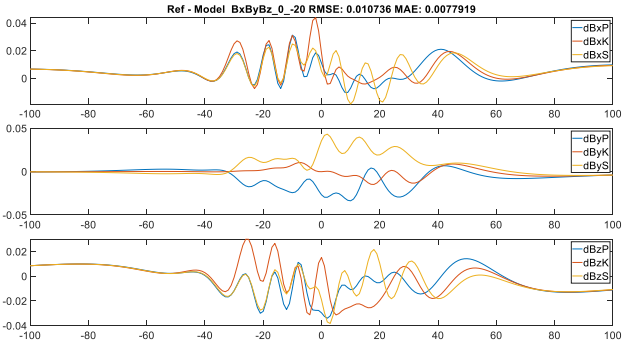

FIGURE 36. Ref-model differences on paths in nT: S3, direction 0.

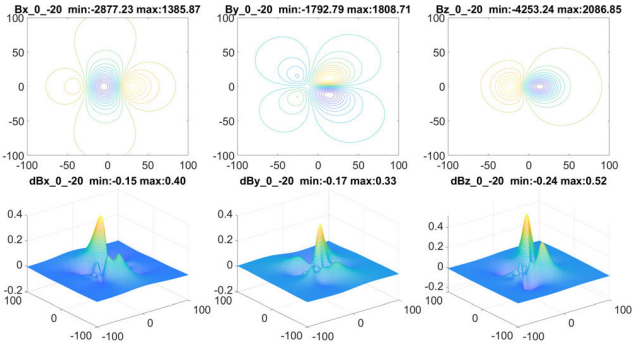

FIGURE 37. Ref-model differences on fields in nT: S3, direction 0.

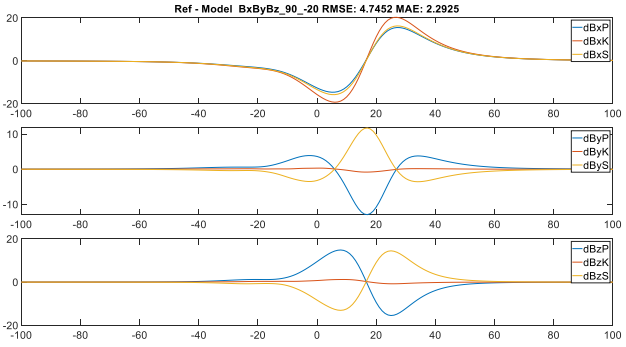

FIGURE 38. Ref-model differences on paths in nT: S3, direction 90.

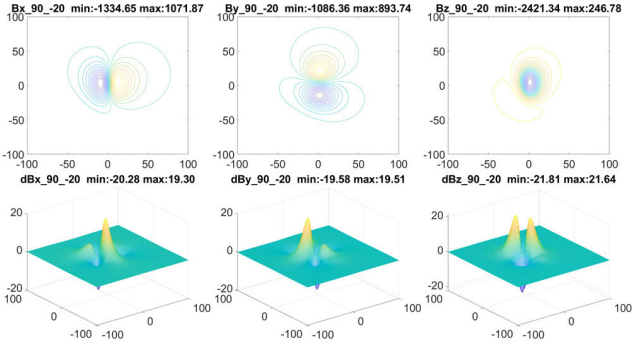

FIGURE 39. Ref-model differences on fields in nT: S3, direction 90.

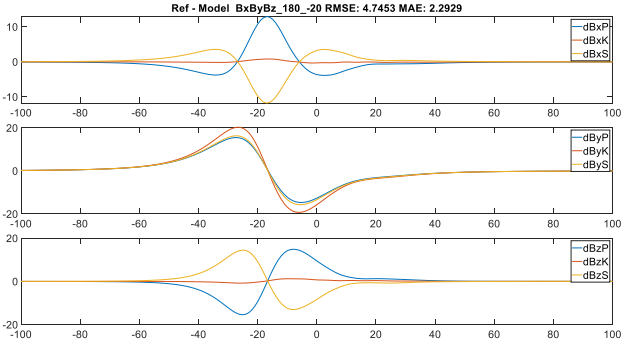

FIGURE 40. Ref-model differences on paths in nT: S3, direction 180.

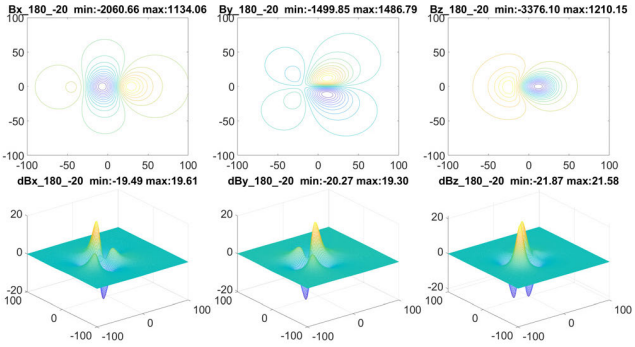

FIGURE 41. Ref-model differences on fields in nT: S3, direction 180.

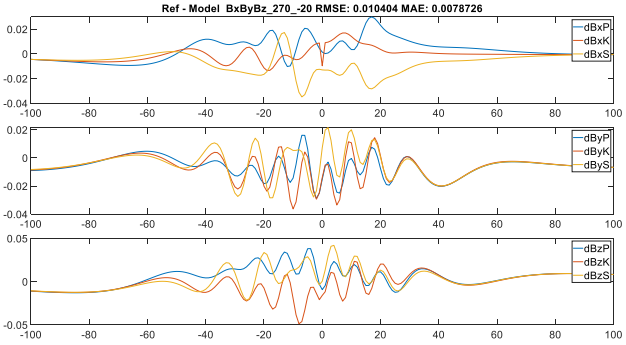

FIGURE 42. Ref-model differences on paths in nT: S3, direction 270.

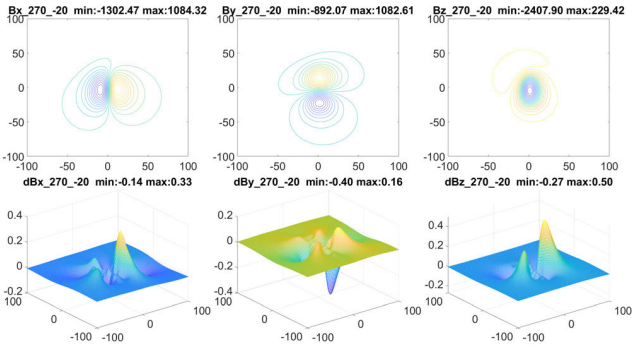

FIGURE 43. Ref-model differences on fields in nT: S3, direction 270.

E. SCENARIO 4: N, E–DIRECTIONS, B_X, B_Y, B_Z DATA, Y FREE, NOISE 1NT

See Figure 44 to 51 here.

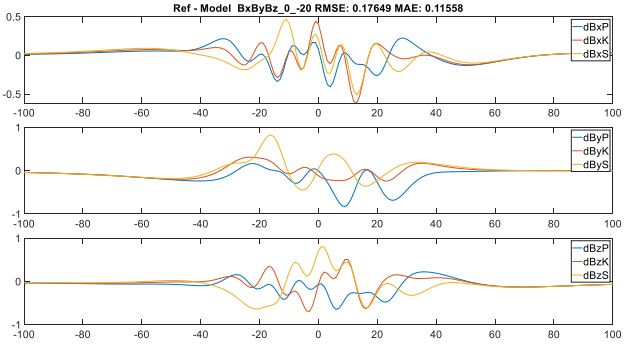

FIGURE 44. Ref-model differences on paths in nT: S4, direction 0.

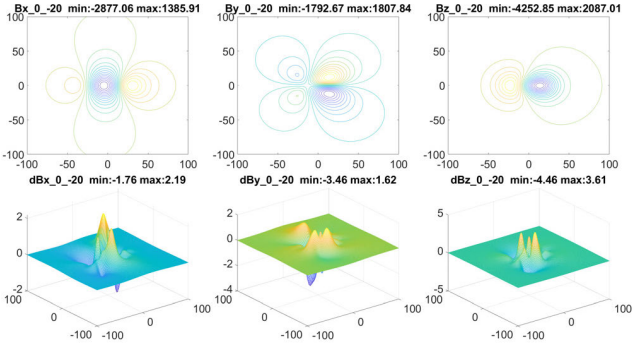

FIGURE 45. Ref-model differences on fields in nT: S4, direction 0.

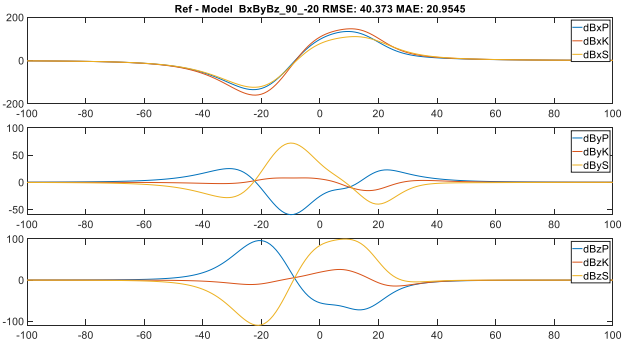

FIGURE 46. Ref-model differences on paths in nT: S4, direction 90.

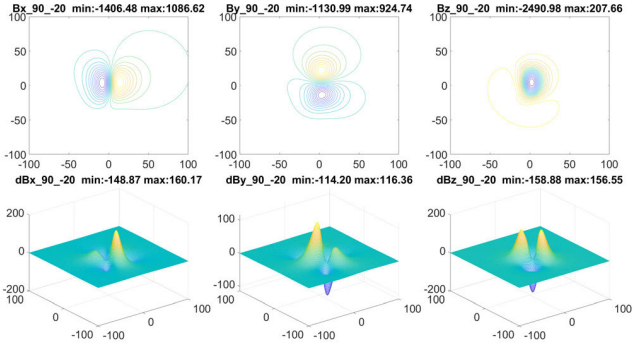

FIGURE 47. Ref-model differences on fields in nT: S4, direction 90.

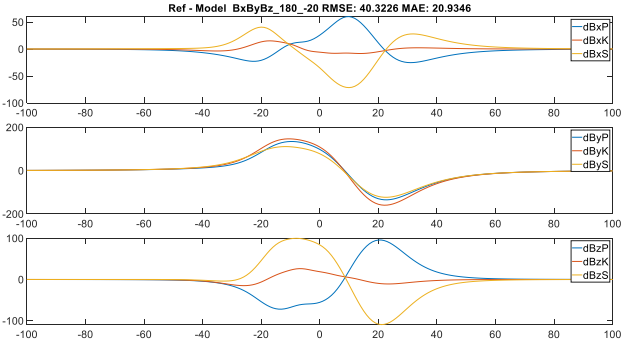

FIGURE 48. Ref-model differences on paths in nT: S4, direction 180.

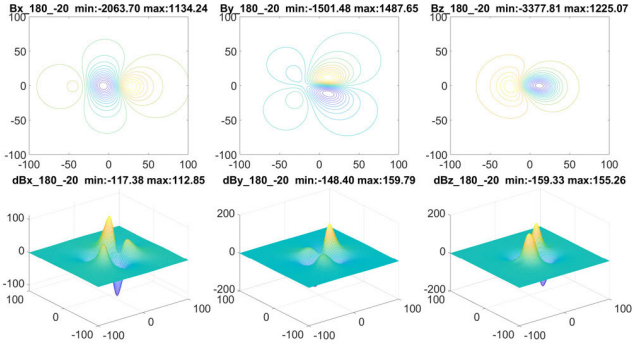

FIGURE 49. Ref-model differences on fields in nT: S4, direction 180.

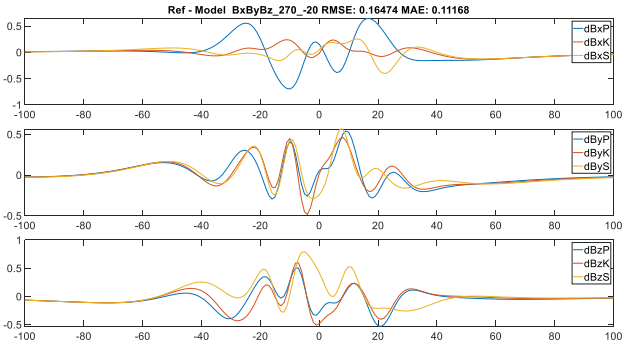

FIGURE 50. Ref-model differences on paths in nT: S4, direction 270.

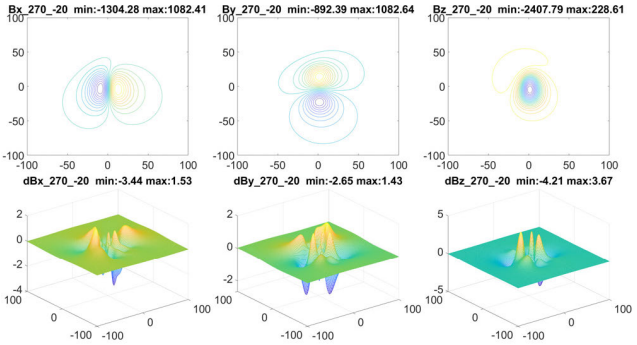

FIGURE 51. Ref-model differences on fields in nT: S4, direction 270.

ACKNOWLEDGMENT

The authors would like to thank the LINTE^2 Laboratory for providing its hardware-software infrastructure.

REFERENCES

[1] F. Le Dorze, J. P. Bongiraud, J. L. Coulomb, P. Labie, and X. Brunotte, "Modeling of degaussing coils effects in ships by the method of reduced scalar potential jump," *IEEE Trans. Magn.*, vol. 34, no. 5, pp. 2477–2480, Sep. 1998.

[2] M. Birsan and R. Tan, "The effect of roll and pitch motion on ship magnetic signature," *J. Magn.*, vol. 21, no. 4, pp. 503–508, Dec. 2016.

[3] I. M. N. Hasril Nain, M. C. Isa, M. M. Muhammad, N. Hassanuddin, N. Yusoff, and M. S. D. Yati, "Management of naval vessels' electromagnetic signatures: A review of sources and countermeasures," *Defence S&T Tech. Bull.*, vol. 6, no. 2, pp. 93–110, 2013.

[4] J. J. Holmes, "Reduction of a ship's magnetic field signatures," *Synth. Lectures Comput. Electromagn.*, vol. 23, pp. 1–76, Jan. 2008.

[5] I. Gloza, S. J. Malinowski, and B. Marchalewski, "Ranges and equipment for the measurement of the ship's underwater signatures," *Hydroacoustics*, vol. 15, pp. 39–48, 2012.

[6] D. P. Benjamin Armstrong, J. Pentzer, D. Odell, T. Bean, J. Canning, J. Frenzel, M. Anderson, and D. Edwards, "Field measurement of surface ship magnetic signature using multiple AUVs," in *Proc. OCEANS*, Oct. 2009, pp. 1–9.

[7] X. Brunotte, G. Meunier, and J.-P. Bongiraud, "Ship magnetizations modelling by the finite element method," *IEEE Trans. Magn.*, vol. 29, no. 2, pp. 1970–1975, Mar. 1993.

[8] F. Le Dorze, J. P. Bongiraud, J. L. Coulomb, P. Labie, and X. Brunotte, "Modeling of degaussing coils effects in ships by the method of reduced scalar potential jump," *IEEE Trans. Magn.*, vol. 34, no. 5, pp. 2477–2480, Sep. 1998.

[9] O. Chadebec, J. Coulomb, V. Leconte, J. P. Bongiraud, and G. Cauffet, "Modeling of static magnetic anomaly created by iron plates," *IEEE Trans. Magn.*, vol. 36, no. 4, pp. 667–671, Jul. 2000.

[10] P. Jankowski and M. Woloszyn, "Applying of thin plate boundary condition in analysis of ship's magnetic field," *COMPEL-Int. J. Comput. Math. Electr. Electron. Eng.*, vol. 37, no. 5, pp. 1609–1617, Sep. 2018.

[11] T.-S. Nguyen, J.-M. Guichon, O. Chadebec, P. Labie, and J.-L. Coulomb, "Ships magnetic anomaly computation with integral equation and fast multipole method," *IEEE Trans. Magn.*, vol. 47, no. 5, pp. 1414–1417, May 2011.

[12] J. McFee and Y. Das, "Fast nonrecursive method for estimating location and dipole moment components of a static magnetic dipole," *IEEE Trans. Geosci. Remote Sens.*, vol. GE-24, no. 5, pp. 663–673, Sep. 1986.

[13] Z. Koczkowski, "Metoda doboru warunku amplitudowego dla kanału magnetycznego układu niekontaktowego z wykorzystaniem aproksymacji pola magnetycznego związanego z okrętem," Ph.D. dissertation, Dept. Elect. Eng., Gdańsk Univ. Technol., Gdańsk, Poland, 1987.

[14] G. Rosu, G. Samoilescu, O. Baltag, A. Bordianu, and A. Ciuculin, "Assessment of the ellipsoidal shell model for ship magnetic signature," in *Proc. 9th Int. Symp. Adv. Topics Electr. Eng. (ATEE)*, May 2015, pp. 413–416.

[15] K. Jakubiuk, P. Zimny, and M. Wołszyn, "Multidipoles model of ship's magnetic field," *Int. J. Appl. Electromagn. Mech.*, vol. 39, nos. 1–4, pp. 183–188, Sep. 2012.

[16] G. Jeung, C.-S. Yang, H.-J. Chung, S.-H. Lee, and D.-H. Kim, "Magnetic dipole modeling combined with material sensitivity analysis for solving an inverse problem of thin ferromagnetic sheet," *IEEE Trans. Magn.*, vol. 45, no. 10, pp. 4169–4172, Oct. 2009.

[17] J.-O. Hall, H. Claesson, J. Kjall, and G. Ljungdahl, "Decomposition of ferromagnetic signature into induced and permanent components," *IEEE Trans. Magn.*, vol. 56, no. 2, pp. 1–6, Feb. 2020.

[18] J. Wang, Y. Shen, R. Zhao, C. Zhou, and J. Gao, "Estimation of dipole magnetic moment orientation based on magnetic signature waveform analysis by a magnetic sensor," *J. Magn. Magn. Mater.*, vol. 505, Jul. 2020, Art. no. 166761.

[19] O. Chadebec, J.-L. Coulomb, J.-P. Bongiraud, G. Cauffet, and P. Le Thiec, "Recent improvements for solving inverse magnetostatic problem applied to thin shells," *IEEE Trans. Magn.*, vol. 38, no. 2, pp. 1005–1008, Mar. 2002.

[20] A. A. Kaufman and D. Alekseev, "Principles of electromagnetic methods in surface geophysics," in *Methods in Geochemistry and Geophysics*, vol. 45. Amsterdam, The Netherlands: Elsevier, 2014.

[21] J. J. Holmes, "Modeling a ship's ferromagnetic signatures," *Synth. Lectures Comput. Electromagn.*, vol. 16, pp. 1–80, Jan. 2007.

[22] *Magnetic Signature Measurement–Bartington Instruments*. Accessed: Sep. 1, 2020. [Online]. Available: https://www.bartington.com/magnetic-signature-measurement/

[23] *MATLAB and Simulink–MathWorks*. Accessed: Sep. 1, 2020. [Online]. Available: https://www.mathworks.com

JAROSLAW TARNAWSKI was born in Gdańsk, in 1974. He received the M.Sc. and Ph.D. degrees from the Gdańsk University of Technology, in 2000 and 2006, respectively. He was a Supervisor with the Computer Control Systems Laboratory, Industrial Class Infrastructure, including DCS, PLC, SCADA systems, and industrial IT networks. He has experience in control of drinking water supply systems and nuclear power control systems. He is currently an Assistant Professor with the Department of Electrical Engineering, Control Systems and Computer Science, Gdańsk University of Technology. His research interests include mathematical modelling, identification, optimization, hierarchical control systems, and adaptive and predictive control for objects with time-varying delays.

ADAM CICHOCKI was born in Opole, in 1971. He received the M.S.Eng. degree in navigation and the Ph.D. degree from the Polish Naval Academy, in 2001. Since 2001, he has been an Adjunct Professor with the Naval Weapons Department, Polish Naval Academy. He is involved in several national and international military and defense research projects. His research interests include oscillate around underwater weapons systems and anti-submarine warfare, especially focused on remote sensing of underwater objects, exploiting their physical fields, such as acoustic, magnetic, and hydrodynamic using passive, and active detection methods.

TOMASZ ADAM RUTKOWSKI was born in Gdańsk, Poland, in 1974. He received the M.Sc. degree in automatics and robotics and the Ph.D. degree in automatic control from the Gdańsk University of Technology, Poland, in 2000 and 2004, respectively. He has experience in control systems of critical infrastructure, such as environmental systems (drinking water distribution systems and wastewater treatment plant systems) and power systems, including nuclear power plants. He is currently an Associate Professor with the Department of Electrical Engineering, Control Systems and Computer Science, Gdańsk University of Technology. His current research interests include mathematical modelling, advanced control algorithms, estimation algorithms, computational intelligence techniques, and industrial control systems.

KRYSTIAN BUSZMAN was born in Koscierzyna, in 1983. He received the M.Sc. degree in electronic and telecommunication engineering from the Gdańsk University of Technology, in 2007. He is currently pursuing the Ph.D. degree in civil engineering and transport with the Polish Naval Academy. From 2007 to 2017, he was an Electronic Engineer with the Hydroacoustic Department, Polish Naval Academy, where he has been a Research Assistant with the Faculty of Navigation and Naval Weapons, since 2017. He is currently a Researcher in number of international and national projects. His research interests include underwater observations of environment and objects in different physical field aspects. He has been a member of the Polish Acoustical Society since 2008.

MIROSLAW WOLOSZYN was born in Gdynia, in 1963. He received the M.Sc., Ph.D., and D.Sc. (Habilitation) degrees from the Gdańsk University of Technology, in 1987, 1997, and 2013, respectively. Since 1987, he has been with the Gdańsk University of Technology, where he is currently an Associate Professor of electrical engineering. He is also a Principal Investigator in national project and a lead researcher in several other national projects. He has authored or coauthored over 150 scientific and technical articles. His research interests include localization and identification of ferromagnetic objects by means of magnetometric method, magnetometric systems for object detection, ship degaussing systems, and measurement systems for ship-induced physical fields. He has been a member of the Polish Society for Theoretical and Applied Electrical Engineering since 1997.